frontiers | Frontiers in Catalysis

TYPE Original Research
PUBLISHED 30 August 2022
DOI 10.3389/fctls.2022.915971

OPEN ACCESS

EDITED BY
Fang-Xing Xiao,
Fuzhou University, China

REVIEWED BY
Hyung Chul Ham,
Inha University, South Korea
Michele Melchionna,
University of Trieste, Italy

*CORRESPONDENCE
Shao-Hui Hsu,
shaohuihsu@narlabs.org.tw
Sung-Fu Hung,
sungfuhung@nycu.edu.tw

†These authors have contributed equally to this work

SPECIALTY SECTION
This article was submitted to Electrocatalysis, a section of the journal Frontiers in Catalysis

RECEIVED 08 April 2022
ACCEPTED 03 August 2022
PUBLISHED 30 August 2022

CITATION
Lu Y-H, Tsai H-J, Huang W-Y, Lee T-J, Lin Z-Y, Hsu S-H and Hung S-F (2022), A nitrogen-doped graphene-supported nickel-single-atom catalyst in the flow cell meets the industrial criteria of carbon dioxide reduction reaction to carbon monoxide.
Front. Catal. 2:915971.
doi: 10.3389/fctls.2022.915971

A nitrogen-doped graphene-supported nickel-single-atom catalyst in the flow cell meets the industrial criteria of carbon dioxide reduction reaction to carbon monoxide

Yi-Hsuan Lu[1†], Hsin-Jung Tsai[1†], Wen-Yang Huang[1], Tsung-Ju Lee[1], Zih-Yi Lin[1], Shao-Hui Hsu[2*] and Sung-Fu Hung[1*]

[1]Department of Applied Chemistry, National Yang Ming Chiao Tung University, Hsinchu, Taiwan, [2]Taiwan Semiconductor Research Institute, National Applied Research Laboratories, Hsinchu, Taiwan

Carbon dioxide reduction reaction (CO_2RR) is a promising approach to accomplishing net zero CO_2 emissions. Among CO_2RR catalysts, nitrogen-doped graphene-supported single-atom catalysts show a remarkable conversion rate from CO_2 to CO; however, the low production amount has been limited using the conversion H cell, hindering its industrial development. In this work, we synthesize a nitrogen-doped graphene-supported nickel-single-atom catalyst and conduct CO_2RR in a flow cell, exhibiting a CO_2-to-CO Faradaic efficiency of 96% and a partial current density of 144 mA cm^{-2}. It can also achieve the highest partial current density of 204 mA cm^{-2} with a turnover frequency of 7,852 h^{-1}. According to the techno-economic analysis, these preeminent activities meet the industrial criteria (Faradaic efficiency >60% and partial current density >100 mA cm^{-2}). This activity enhancement using a flow system can significantly accelerate net-zero CO_2 emission realization.

KEYWORDS

carbon dioxide reduction, single atom catalyst, carbon monoxide, flow cell, industrial criteria

Introduction

According to the Paris Agreement in 2015, to reduce global warming and climate change, carbon emissions require to be reduced by 45% from 2010 levels by 2030 and reach net zero by 2050. Carbon dioxide reduction reaction (CO_2RR) has been regarded as a potential way to achieve net zero CO_2 emissions (Birdja et al., 2019; Nitopi et al., 2019; Hung, 2020a; Overa et al., 2022). Electrochemical CO_2RR can also obtain various

economic products, such as carbon monoxide, ethylene, and ethanol, leading to the consideration of industrialization (Nitopi et al., 2019; Spurgeon and Kumar, 2018). Among these products, carbon monoxide, instead of greenhouse gas, is a crucial reactant in Fischer-Tropsch process and metallurgy. The price of CO reaches over 1,300 USD tC^{-1}. Therefore, CO_2 to CO product can eliminate the atmospheric CO_2 and facilitate the chemical and metallurgical industry.

Recently, the nitrogen-doped graphene-supported single-atom catalysts present superior CO_2RR activity towards the CO product (Ju et al., 2017; Su et al., 2019; Liu et al., 2020; Li et al., 2022). The atomic active sites are bound on the conductive nitrogen-doped carbon substrates to facilitate the electron transfer, while the electronic configuration of the metal centers can improve the CO_2 activation (Yang et al., 2018; Li et al., 2019; Vijay et al., 2021). The continuous sp^2 carbon atom network promotes the charge flow and electron mobility of the substrate (Melchionna et al., 2021). The carbon substrate with a high surface area, ranging from 100–1,000 $m^2 g^{-1}$, also provides abundant electrocatalytic sites to enhance the catalytic activity. Yang et al. (2018) reported a single-Ni-atom catalyst exhibiting CO_2-to-CO Faradaic efficiency of 97% and a partial current density of 22 mA cm^{-2} at a mild overpotential of 0.61 V in an H-cell. Nearly all the provided electrons reduce CO_2 to CO rather than generate hydrogen. The selectivity of single-atom catalysts is significantly higher than the conventional noble metal catalysts (Hori et al., 1994). However, the low current density obstructs its industrial development.

Regarding the industrial application of CO_2RR, the techno-economic analysis, including capital and operating costs for the CO_2 electrolysis process, should be further considered (Jouny et al., 2018; Spurgeon and Kumar, 2018). For C1 products, such as CO and formic acid, it is profitable as the selectivity reaches 60% Faradaic efficiency and the partial current density for the single product comes to 100 mA cm^{-2}. Thus, the selectivity of single-atom catalysts achieves the goal, but the partial current density misses the goal if using an H cell, in which insufficient CO_2 can be catalyzed due to the poor solubility in the electrolyte. A flow cell enables CO_2 to reach the catalyst surface directly without purging CO_2 into the electrolyte to augment the local CO_2 concentration to promote overall catalytic activity (Li et al., 2020; Wang et al., 2020; Xu et al., 2021; Hung et al., 2022).

Herein, we prepared a nitrogen-doped graphene-supported nickel-single-atom catalyst (NiNG) and catalyzed CO_2 in a flow cell. It achieved a CO_2-to-CO Faradaic efficiency of 96% and a partial current density of 144 mA cm^{-2}. It also achieved the highest partial current density of 204 mA cm^{-2}. These CO_2RR performances met the industrial criteria. Compared to nickel phthalocyanine (NiPc, similar molecular structure of the central metal to NiNG), the graphited carbon around the central nickel in NiNG regulated the electronic configuration and oxidation number of the central nickel, which determines the CO_2RR selectivity, identified by X-ray absorption spectroscopy and Raman spectrum. The enhanced CO_2RR activity of NiNG in the flow cell would boost the progress of net zero CO_2 emissions.

Results and discussion

We synthesized NiNG by a two-step pyrolysis process under the Ar atmosphere, followed by an acid washing process to remove undesirable Ni aggregation. NiNG showed a sheet-like porous nanostructure, shown in Figures 1A,B. The dimension of the nanosheet extended to the scale of several μm. The broad peaks near 25.4° and 43.3° of XRD in Supplementary Figure S1 were referred to (002) and (101) facets of graphite (Xu et al., 2018). The crystallized metallic Ni or NiO was not detected. We performed high-angle annular dark-field scanning transmission electron microscopy with Cs-corrector (HAADF-STEM), displaying considerable bright spots with the atom size without observing nanoparticles or clusters (Figure 1C).

We further conducted extended X-ray absorption fine structure (EXAFS) to confirm the single-atom nature and the coordination environment of NiNG (Frenkel, 2012; Hung, 2020b). In Figure 1D, the major peak of NiNG around 1.4 Å (without phase correction) can be attributed to the Ni-N scattering path, similar to the Ni-N coordination of NiPc, whose molecular configuration was shown in Supplementary Figure S2 (Ren et al., 2019; Liu et al., 2020). We did not observe the peak around 2.1 Å (the metallic Ni-Ni scattering path) in NiNG. As nickel compounds exhibit considerably smaller EXAFS peaks than the nickel metal, we further performed wavelet analysis to identify the energy dependence of each EXAFS peak (Figures 1E,F; Supplementary Figure S3). NiNG features only one region of signals that centers at 5.5 $Å^{-1}$, consistent with the Ni-N coordination in the EXAFS result. Two regions of signals at 2.1 Å and 4.5 Å centering at 7.2 $Å^{-1}$ in Ni foil, meaning that the interaction is between the elements with relatively high molecular weight, i.e., Ni-Ni. Hence, we affirmed the atomic dispersion of nickel in NiNG, consistent with the AR-TEM result in Figure 1C. Interestingly, the wavelet contour of NiNG was divergent from NiPc (four regions of signals that centers at 6 $Å^{-1}$, 4.5 $Å^{-1}$, and 3.5 $Å^{-1}$ in Supplementary Figure S4). It unveils the different surrounding carbon coordination of NiNG from NiPc. Raman spectroscopy in Supplementary Figure S5 also showed that NiNG is partially graphitized and subsequently possesses superb electrical conductivity, but NiPc holds the organic carbons from the phthalocyanine ring (Liu et al., 2007; Li et al., 2015; Zhao et al., 2019).

The valence orbitals of C can be influenced by the graphitization, identified *via* C K-edge XAS (Figure 2A). The peaks at 284.8 and 291.7 eV in NiNG corresponded to the 1s-π^* and 1s-σ^* transitions of sp^2-bonded C, respectively, verifying the graphite carbons in NiNG (Ehlert et al., 2014). On the other hand, the peaks at 286.2 and 287.4 eV in NiPc represent the 1s excitations to π^* orbitals of two non-equivalent carbon atoms (C=C, and C=N) within the pyrrole subunits (Milev et al., 2007; Mauerer et al., 1993).

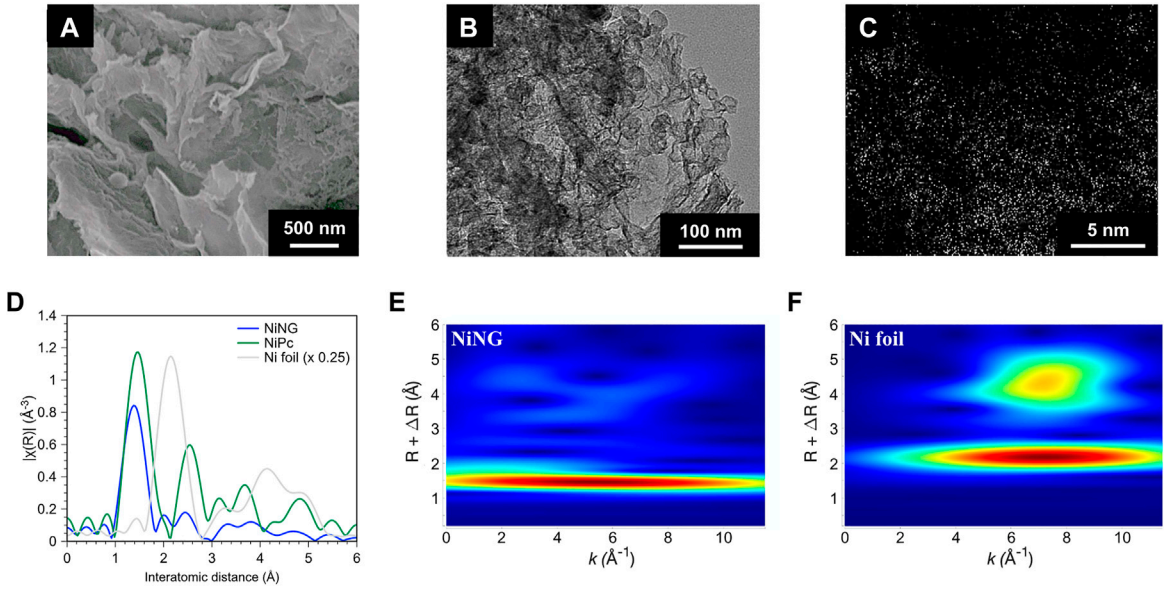

FIGURE 1
Structural identification of NiNG. **(A)** SEM and **(B)** TEM image of NiNG. **(C)** Cs-corrected HAADF-STEM image of NiNG. **(D)** Ni K-edge EXAFS spectra of NiNG and the standard of Ni foil and NiPc. Wavelet analysis of the k^2-weight EXAFS spectra of **(E)** NiNG and **(F)** Ni foil as reference.

The peak at 289.2 eV can be assigned to overlapped π* + σ* excitations. Thus, the valence orbitals of C in NiNG and NiPc are pretty different. They also affect the valence orbitals of N, shown in Figure 2B. The peaks at 398.8 and 400.8 eV express the excitations to π* orbitals of two non-equivalent nitrogen atoms (the pyridinic N and graphitic N). The peak of graphitic N is higher than the pyridinic N, indicating the dominated graphitic N in NiNG. The peaks at 406.5 eV in NiNG can be appointed to the σ* excitations (Zhu et al., 1997). The peaks in NiPc contribute from the π* excitations of two different nitrogen atoms: one locates at the pyrrole rings surrounding the metal, and the other is at the meso positions of the macrocyclic ring (De Francesco et al., 2012).

Divergent valence orbitals of N near the central Ni also affect those of central Ni, unveiled by the shifted L_3/L_2 peaks of NiNG in Ni L-edge XAS (Figure 2C). They also influence the oxidation number of Ni in NiNG. To identify the oxidation number in NiNG, we conducted Ni K-edge XANES and analyzed the first-order derivatives of XANES spectra in Figure 2D; Supplementary Figure S6, along with Ni foil and NiO standards. The average oxidation number of NiNG is 0.8, while that of NiPc is higher than 2, consistent with the Ni L-edge XAS result. The properties of central Ni will determine the catalytic behavior of NiNG for CO_2RR.

We prepared the gas diffusion electrode (GDE) by spray-coating NiNG on the Ti/PTFE substrate and investigated CO_2RR performance in 1 M $KHCO_3$ in a flow cell, illustrated in Figure 3A; Supplementary Figure S7. Instead of dissolving scarce CO_2 (5% solubility) into electrolyte to perform CO_2RR in a H-cell, an additional gas chamber in a flow cell provides pure CO_2 to the catalyst surface, increasing local CO_2 concentration, promoting overall CO_2RR activity. Benefited from the flow cell, NiNG can produce major CO and maintain the Faradaic efficiency higher than 90%, even exerting the current density of 200 mA cm^{-2} (Figure 3B), overperforming the CO_2RR activities in a H cell (Supplementary Table S1) (Ju et al., 2017; Zhao et al., 2017; Hu et al., 2018; Yang et al., 2018; Liu et al., 2020; Sa et al., 2020). We identified the ^{13}CO production in a flow cell using $^{13}CO_2$ as feedstock, confirming that the CO evolves from CO_2 rather than $KHCO_3$ (Supplementary Figure S8).

In comparison to NiNP/NG (Ni nanoparticles on NG), bared NG, and NiPc (Figure 3C), NiNG can effectively produce CO at wide range of applied current densities, while NiNP/NG only produces CO at the relatively low current density. We attributed the selectivity to the H/CO affinity of Ni domain size (Hung et al., 2022). Bared NG was unable to produce CO, evidencing that single-atom nickel is the active site of CO_2RR toward CO production. NiPc also failed to produce CO even the similar molecular structure of the central metal to NiNG, shown in Supplementary Figure S2. The graphited carbons around the central nickel in NiNG can regulate the electronic configuration, oxidation number of the central nickel, and they lower the adsorption energy of the *COOH intermediates during CO_2RR to facilitate CO production (Yang et al., 2018). NiNG achieved a CO_2-to-CO Faradaic efficiency of 96% and a partial current density of 144 mA cm^{-2}, which meets the industrial criteria according to the techno-economic analysis. It is worth mentioning that a CO_2-to-CO FE of 81.5% and a partial current

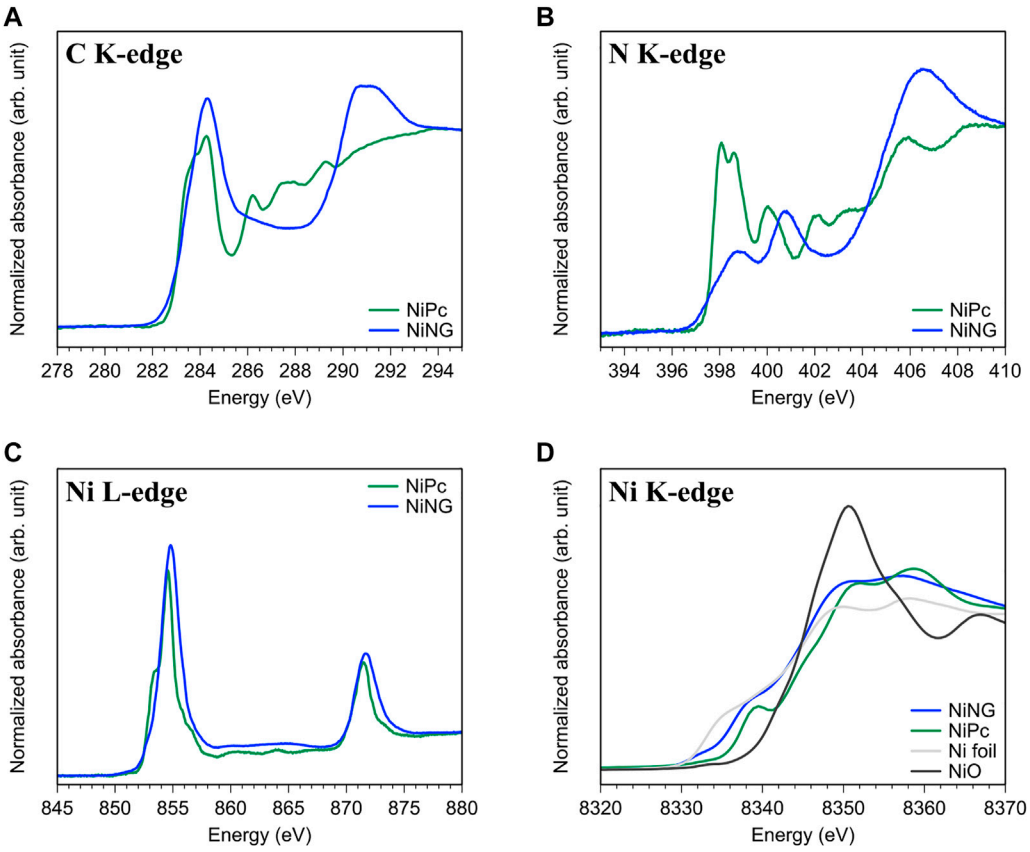

FIGURE 2
Chemical characterization of NiNG. **(A)** C K-edge, **(B)** N K-edge and **(C)** Ni L-edge XANES spectra of NiNG. **(D)** Ni K-edge XANES spectra of NiNG.

density of 204 mA cm^{-2} can be achieved at a current density of 250 mA cm^{-2} (Figure 3D). The present system gives a ×6.5 to ×9.3 higher partial current density than our previous report (Yang et al., 2018), suggesting the merits of using a flow cell. The remarkable partial current density is attributed to the larger applied current density, which benefits from a high local CO_2 concentration near the catalyst surface. The loading amount of NiNG on the GDE also determines the highest applied current density (Supplementary Figure S9). NiNG with loading amounts of 0.5 mg cm^{-2}, 1.0 mg cm^{-2}, and 1.5 mg cm^{-2} preserved the Faradaic efficiency higher than 95% at the current density of 50 mA cm^{-2}, 100 mA cm^{-2}, 150 mA cm^{-2}, respectively, significantly higher than the optimized loading amounts of 0.1 mg cm^{-2} in H cell, which results in a low applied current density (Yang et al., 2018). The cyclic voltammetry of NiNG (Supplementary Figure S10) revealed no obvious redox pairs, meaning the sustainable chemical state during CO_2RR.

The best performance in this work (a CO_2-to-CO Faradaic efficiency of 96% and a partial current density of 144 mA cm^{-2}) was acquired at an overpotential of 0.825 V, while the highest partial current density achieves at the overpotential of 0.881 V (Figure 3E). Tafel slope of 243 mV dec^{-1} (higher than the theoretical Tafel slope of 120 mV dec^{-1}) was obtained for NiNG (Supplementary Figure S11), indicating that the first electron transfer to form a CO_2^- anion radical is the rate-determining step for CO evolution (Gattrell et al., 2006). Turnover frequency (TOF) was evaluated by calculating the turnover number for CO formation per active site. The number of nickel active sites was collected by ICP-MS (1.894 wt% in NiNG). TOF was found to increase with the applied current density (Figure 3F). NiNG achieved the highest TOF of 7,852 h^{-1} at the overpotential of 881 V. The polarization curve of NiNG in the flow cell after 10,000 CV cycles was similar to that in the initial state (Figure 3G), revealing the stable catalytic nature of NiNG in the flow cell. NiNG in the flow cell can catalyze sufficient CO_2 to CO, achieving high selectivity, high partial current density, high turnover frequency, and high stability towards generating CO to reach the industrial level for CO_2RR.

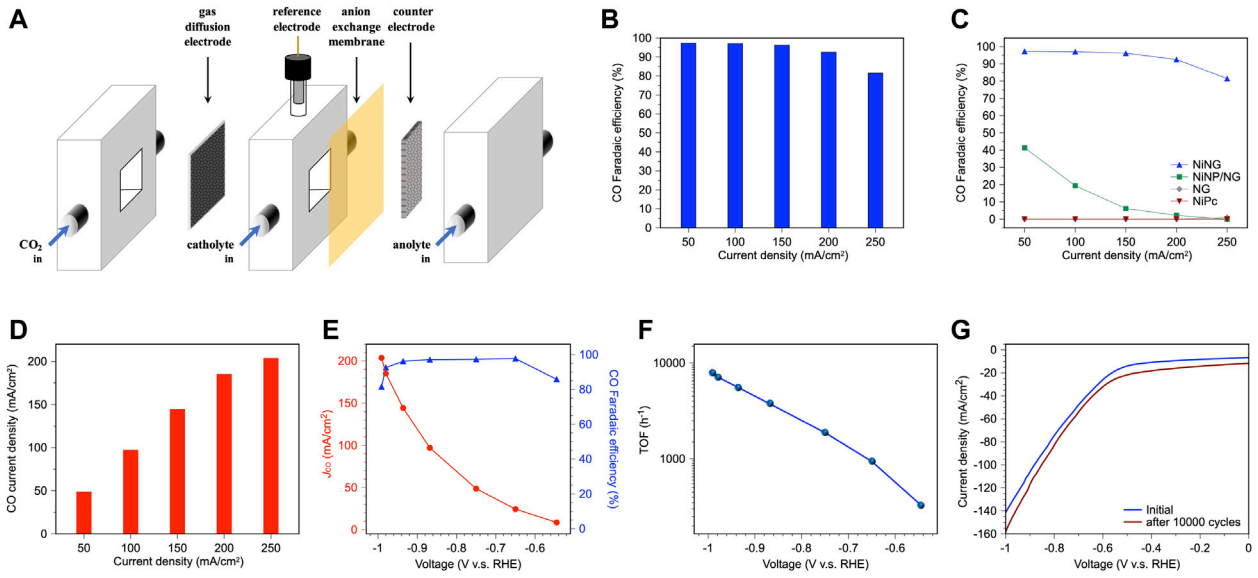

FIGURE 3
Catalytic performance of NiNG in the flow cell. **(A)** Schematic illustration of the flow cell. **(B)** CO faradaic efficiency of NiNG at various current densities for CO_2RR. **(C)** The comparison of CO faradaic efficiency of NiNG with NiNP/NG, NG, and NiPc. **(D)** CO current density of NiNG at various current densities for CO_2RR. **(E)** CO Faradaic efficiency and partial current density vs. applied potential of NiNG with the loading amount of 1.5 mg/cm^2. **(F)** TOF of NiNG for CO production of CO_2RR. **(G)** Polarization curve of NiNG during CO_2RR before and after 10,000 CV cycles.

Conclusion

We developed a CO_2RR catalytic system of a nitrogen-doped graphene-supported nickel-single-atom catalyst in a flow cell. A CO_2-to-CO Faradaic efficiency of 96% and a partial current density of 144 mA cm^{-2} reaching the industrial level were demonstrated. The highest partial current density of 204 mA cm^{-2} with a turnover frequency of 7,852 h^{-1} in this system makes it profitable. The graphited carbons and lower oxidation number of the central nickel in NiNG facilitated the CO generation during CO_2RR. Benefited from the flow cell, sufficient CO_2 concentration near the catalyst surface accelerated the entire catalytic rate to enhance the current density and partial current density. The present system allows us to develop CO_2RR industrialization and reach the goal of net-zero CO_2 emission in the near future.

Materials and methods

Synthesis of a nitrogen-doped graphene-supported nickel-single-atom catalyst

In a typical synthesis of a nitrogen-doped graphene-supported nickel-single-atom catalyst (NiNG), a mixture of melamine ($C_3H_6N_6$) (12 g), l-alanine ($C_3H_7NO_2$) (2.25 g), and nickel (ii) acetate tetrahydrate ($Ni(CH_3COO)_2{\cdot}4H_2O$) (0.2 g) was first ground into a homogeneous precursor using zirconia ball in a nylon jar. Subsequently, the fine powder mixture underwent a two-stage pyrolysis and carbonization process (first stage: from 25 to 600°C at a ramping rate of 3°C min^{-1}, maintain at 600°C for 2 h; second stage: from 600 to 900°C at a ramping rate of 2°C min^{-1}, maintain at 900°C for 1 h) in a tubular furnace (Carbolite, United Kingdom) in the argon atmosphere. After cooling down to room temperature, the product was successively leached at 80°C in 1 M HCl for 12 h and 1 M HNO_3 for another 24 h to remove metal particles and unstable species. Afterwards, the sample was heated again at 850°C in Ar for 1 h to recover the crystallinity of carbon.

Sprayed coating of nickel-single-atom catalyst on Ti/PTFE substrate

The 6 mg of NiNG was mixed with 24 μl of Nafion solution (~5 wt%) and 300 μl of methanol. This dispersed ink was sprayed onto a Ti/PTFE substrate with a size of 2 cm × 2 cm and an area loading of 1.5 mg cm^{-2}.

Characterization

Microstructure was collected by field-emission scanning electron microscopy (FESEM, JEOL, JSM-6500F) equipped

energy dispersive X-ray spectroscopy (EDX, Oxford Instrument XMax 150 mm^2). Cold-field emission Cs-corrected transmission electron microscope (JEOL ARM-200F) with 200 keV acceleration voltage was used in microstructure analysis. The crystallization of materials was assessed using a Bruker D8 Advance X-ray diffraction (XRD) analyzer with Cu Kα radiation (λ = 1.5406 Å). Raman spectra were recorded by Renishaw inVia Raman microscope—A Raman microscopy system, employing a diode laser at 785 nm. A ×50 objective lens was used to focus the laser on the sample. X-ray absorption spectroscopy (XAS) including X-ray absorption near edge spectra (XANES) and extended X-ray absorption fine structure (EXAFS) of Cu K-edge were collected in fluorescence mode using a Lytle detector at the BL17C beamline in NSRRC. The pre-edge baseline was subtracted and the spectra was normalized to the post-edge. EXAFS analysis was conducted using a Fourier transform on k2-weighted EXAFS oscillations to evaluate the contribution of each bond pair to the Fourier transform peak.

Electrochemical measurement

Electrochemical properties were investigated using a Biologic VSP-3e potentiostat in a flow cell reactor using a gas diffusion electrode (GDE) as the working electrode (WE), nickel foam as the counter electrode (CE), and a saturated Ag/AgCl electrode as the reference electrode (RE). The WE and CE were separated by an anion exchange membrane. An aqueous solution of 1.0 M $KHCO_3$ was used as the electrolyte, and the flow rate of CO_2 was 50 sccm. The potentials were converted to values relative to RHE based on the following equation: $E_{RHE} = E_{Ag/AgCl} + 0.0591 \times pH + E_{0,\ Ag/AgCl}$, where $E_{0,\ Ag/AgCl}$ is the standard potential of Ag/AgCl relative to SHE at 25°C (0.210 V). The working area of electrodes was 1.0 cm^2 for each experiment. Linear sweep voltammetry was performed at the scan rate of 20 mV/s with iR-correction. Cyclic voltammetry was measured at the scan rate of 100 mV/s. The Faradaic efficiencies of gaseous products were evaluated *via* gas chromatography (Agilent 8860) equipped with a thermal conductivity detector and a flame ionization detector. The partial current density for CO product was obtained by the equation: total current density x Faradaic efficiency of CO product. The isotopic CO product using $^{13}CO_2$ was measured *via* GC-MS (Thermo Scientific TRACE Series 1300 GC). TOFs (h^{-1}) for the CO_2RR were evaluated based on the 2-electron pathway for CO. TOF = Turnover number for CO formation/Number of active sites.

Data availability statement

The original contributions presented in the study are included in the article/Supplementary Material, further inquiries can be directed to the corresponding authors.

Author contributions

S-FH and S-HH supervised the project and conceived the idea. Y-HL and H-JT carried out the experiments. S-FH wrote the paper. Y-HL and H-JT carried out the electrochemical experiments. Y-HL and H-JT carried out XAS and wavelet analysis. W-YH conducted and analyzed XRD and SEM. T-JL and Z-YL conducted and analyzed Raman. All authors discussed the results and assisted during manuscript preparation.

Funding

The supports from the Ministry of Science and Technology, Taiwan (Contract No. MOST 110-2113-M-009-007-MY2 and MOST 111-2628-M-A49-007) are gratefully acknowledged.

Acknowledgments

We also thank the support from the Yushan Young Scholar Program, Ministry of Education, Taiwan.

Conflict of interest

The authors declare that the research was conducted in the absence of any commercial or financial relationships that could be construed as a potential conflict of interest.

Publisher's note

Supplementary material

The Supplementary Material for this article can be found online at: https://www.frontiersin.org/articles/10.3389/fctls.2022.915971/full#supplementary-material

References

Birdja, Y. Y., Pérez-Gallent, E., Figueiredo, M. C., Göttle, A. J., Calle-Vallejo, F., and Koper, M. T. M. (2019). Advances and challenges in understanding the electrocatalytic conversion of carbon dioxide to fuels. *Nat. Energy* 4, 732–745. doi:10.1038/s41560-019-0450-y

de Francesco, R., Stener, M., and Fronzoni, G. (2012). Theoretical study of near-edge X-ray absorption fine structure spectra of metal phthalocyanines at C and N K-edges. *J. Phys. Chem. A* 116, 2885–2894. doi:10.1021/jp2109913

Ehlert, C., Unger, W. E., and Saalfrank, P. (2014). C K-edge NEXAFS spectra of graphene with physical and chemical defects: A study based on density functional theory. *Phys. Chem. Chem. Phys.* 16, 14083–14095. doi:10.1039/c4cp01106f

Frenkel, A. I. (2012). Applications of extended X-ray absorption fine-structure spectroscopy to studies of bimetallic nanoparticle catalysts. *Chem. Soc. Rev.* 41, 8163–8178. doi:10.1039/c2cs35174a

Gattrell, M., Gupta, N., and Co, A. (2006). A review of the aqueous electrochemical reduction of CO_2 to hydrocarbons at copper. *J. Electroanal. Chem.* 594, 1–19. doi:10.1016/j.jelechem.2006.05.013

Hori, Y., Wakebe, H., Tsukamoto, T., and Koga, O. (1994). Electrocatalytic process of CO selectivity in electrochemical reduction of CO_2 at metal electrodes in aqueous media. *Electrochimica Acta* 39, 1833–1839. doi:10.1016/0013-4686(94)85172-7

Hu, X.-M., Hval, H. H., Bjerglund, E. T., Dalgaard, K. J., Madsen, M. R., Pohl, M.-M., et al. (2018). Selective CO2 reduction to CO in water using earth-abundant metal and nitrogen-doped carbon electrocatalysts. *ACS Catal.* 8, 6255–6264. doi:10.1021/acscatal.8b01022

Hung, S.-F. (2020a). Electrochemical flow systems enable renewable energy industrial chain of CO_2 reduction. *Pure Appl. Chem.* 92, 1937–1951. doi:10.1515/pac-2020-0705

Hung, S.-F. (2020b). *In-situ* X-ray techniques for non-noble electrocatalysts. *Pure Appl. Chem.* 92, 733–749. doi:10.1515/pac-2019-1006

Hung, S.-F., Xu, A., Wang, X., Li, F., Hsu, S.-H., Li, Y., et al. (2022). A metal-supported single-atom catalytic site enables carbon dioxide hydrogenation. *Nat. Commun.* 13, 819. doi:10.1038/s41467-022-28456-9

Jouny, M., Luc, W., and Jiao, F. (2018). General techno-economic analysis of CO_2 electrolysis systems. *Ind. Eng. Chem. Res.* 57, 2165–2177. doi:10.1021/acs.iecr.7b03514

Ju, W., Bagger, A., Hao, G.-P., Varela, A. S., Sinev, I., Bon, V., et al. (2017). Understanding activity and selectivity of metal-nitrogen-doped carbon catalysts for electrochemical reduction of CO_2. *Nat. Commun.* 8, 944. doi:10.1038/s41467-017-01035-z

Li, C., Ju, W., Vijay, S., Timoshenko, J., Mou, K., Cullen, D. A., et al. (2022). Covalent organic framework (COF) derived Ni-N-C catalysts for electrochemical CO_2 reduction: Unraveling fundamental kinetic and structural parameters of the active sites. *Angew. Chem. Int. Ed. Engl.* 61, e202114707. doi:10.1002/anie.202114707

Li, F., Li, Y. C., Wang, Z., Li, J., Nam, D.-H., Lum, Y., et al. (2020). Cooperative CO_2-to-ethanol conversion via enriched intermediates at molecule–metal catalyst interfaces. *Nat. Catal.* 3, 75–82. doi:10.1038/s41929-019-0383-7

Li, J., Pršlja, P., Shinagawa, T., Martín Fernández, A. J., Krumeich, F., Artyushkova, K., et al. (2019). Volcano trend in electrocatalytic CO_2 reduction activity over atomically dispersed metal sites on nitrogen-doped carbon. *ACS Catal.* 9, 10426–10439. doi:10.1021/acscatal.9b02594

Li, X., Wang, B., Wang, X., Zhou, X., Chen, Z., He, C., et al. (2015). Enhanced NH_3-sensitivity of reduced graphene oxide modified by tetra-α-iso-pentyloxymetallophthalocyanine derivatives. *Nanoscale Res. Lett.* 10, 373. doi:10.1186/s11671-015-1072-3

Liu, S., Yang, H. B., Hung, S.-F., Ding, J., Cai, W., Liu, L., et al. (2020). Elucidating the electrocatalytic CO_2 reduction reaction over a model single-atom nickel catalyst. *Angew. Chem. Int. Ed. Engl.* 59, 808–813. doi:10.1002/ange.201911995

Liu, Z., Zhang, X., Zhang, Y., and Jiang, J. (2007). Theoretical investigation of the molecular, electronic structures and vibrational spectra of a series of first transition metal phthalocyanines. *Spectrochimica Acta Part A Mol. Biomol. Spectrosc.* 67, 1232–1246. doi:10.1016/j.saa.2006.10.013

Mauerer, M., Zebisch, P., Weinelt, M., and Steinrück, H. P. (1993). Resonant excitation and decay of core holes in condensed layers of furan and pyrrole. *J. Chem. Phys.* 99, 3343–3352. doi:10.1063/1.465144

Melchionna, M., Fornasiero, P., Prato, M., and Bonchio, M. (2021). Electrocatalytic CO_2 reduction: Role of the cross-talk at nano-carbon interfaces. *Energy Environ. Sci.* 14, 5816–5833. doi:10.1039/d1ee00228g

Milev, A., Kannangara, G. S. K., Tran, N., and Wilson, M. (2007). Molecular structure reorganisation of Fe-Co- and Ni-phthalocyanines upon milling. *Int. J. Nanotechnol.* 4, 516–522. doi:10.1504/ijnt.2007.014748

Nitopi, S., Bertheussen, E., Scott, S. B., Liu, X., Engstfeld, A. K., Horch, S., et al. (2019). Progress and perspectives of electrochemical CO_2 reduction on copper in aqueous electrolyte. *Chem. Rev.* 119, 7610–7672. doi:10.1021/acs.chemrev.8b00705

Overa, S., Ko, B. H., Zhao, Y., and Jiao, F. (2022). Electrochemical approaches for CO_2 conversion to chemicals: A journey toward practical applications. *Acc. Chem. Res.* 55, 638–648. doi:10.1021/acs.accounts.1c00674

Ren, W., Tan, X., Yang, W., Jia, C., Xu, S., Wang, K., et al. (2019). Isolated diatomic Ni-Fe metal-nitrogen sites for synergistic electroreduction of CO_2. *Angew. Chem. Int. Ed. Engl.* 58, 7046–7050. doi:10.1002/ange.201901575

Sa, Y. J., Jung, H., Shin, D., Jeong, H. Y., Ringe, S., Kim, H., et al. (2020). Thermal transformation of molecular Ni2+–N4 sites for enhanced CO_2 electroreduction activity. *ACS Catal.* 10, 10920–10931. doi:10.1021/acscatal.0c02325

Spurgeon, J. M., and Kumar, B. (2018). A comparative technoeconomic analysis of pathways for commercial electrochemical CO_2 reduction to liquid products. *Energy Environ. Sci.* 11, 1536–1551. doi:10.1039/c8ee00097b

Su, X., Yang, X. F., Huang, Y., Liu, B., and Zhang, T. (2019). Single-atom Catalysis toward efficient CO_2 conversion to CO and formate products. *Acc. Chem. Res.* 52, 656–664. doi:10.1021/acs.accounts.8b00478

Vijay, S., Ju, W., Brückner, S., Tsang, S.-C., Strasser, P., and Chan, K. (2021). Unified mechanistic understanding of CO_2 reduction to CO on transition metal and single atom catalysts. *Nat. Catal.* 4, 1024–1031. doi:10.1038/s41929-021-00705-y

Wang, X., Wang, Z., García de Arquer, F. P., Dinh, C.-T., Ozden, A., Li, Y. C., et al. (2020). Efficient electrically powered CO_2-to-ethanol via suppression of deoxygenation. *Nat. Energy* 5, 478–486. doi:10.1038/s41560-020-0607-8

Xu, Y., Li, F., Xu, A., Edwards, J. P., Hung, S.-F., Gabardo, C. M., et al. (2021). Low coordination number copper catalysts for electrochemical CO_2 methanation in a membrane electrode assembly. *Nat. Commun.* 12, 2932. doi:10.1038/s41467-021-23065-4

Xu, Y., Lu, Y., Zhu, X., and Wang, M. (2018). TE-C36 carbon: A new semiconducting phase with an all-sp^3 bonding network. *RSC Adv.* 8, 1846–1851. doi:10.1039/c7ra11448f

Yang, H. B., Hung, S.-F., Liu, S., Yuan, K., Miao, S., Zhang, L., et al. (2018). Atomically dispersed Ni(i) as the active site for electrochemical CO_2 reduction. *Nat. Energy* 3, 140–147. doi:10.1038/s41560-017-0078-8

Zhao, C., Dai, X., Yao, T., Chen, W., Wang, X., Wang, J., et al. (2017). Ionic exchange of metal–organic frameworks to access single nickel sites for efficient electroreduction of CO_2. *J. Am. Chem. Soc.* 139, 8078–8081. doi:10.1021/jacs.7b02736

Zhao, L., Zhang, Y., Huang, L.-B., Liu, X.-Z., Zhang, Q.-H., He, C., et al. (2019). Cascade anchoring strategy for general mass production of high-loading single-atomic metal-nitrogen catalysts. *Nat. Commun.* 10, 1278. doi:10.1038/s41467-019-09290-y

Zhu, Q., Money, S. L., Russell, A. E., and Thomas, K. M. (1997). Determination of the fate of nitrogen functionality in carbonaceous materials during pyrolysis and combustion using X-ray absorption near edge structure spectroscopy. *Langmuir* 13, 2149–2157. doi:10.1021/la961027s